One-step controllable fabrication of 3D structured self-standing Al_3Ni_2/Ni electrode through molten salt electrolysis for efficient water splitting

Hua, Zhongsheng; Wu, Xiaobin; Zhu, Zengli; He, Jiwen; He, Shiwei; Liu, Huan; Xu, Liang; Yang, Yongxiang; Zhao, Zhuo

DOI
10.1016/j.cej.2021.131743

Publication date
2022

Document Version
Final published version

Published in
Chemical Engineering Journal

Chemical Engineering Journal 427 (2022) 131743

Contents lists available at ScienceDirect

Chemical Engineering Journal

journal homepage: www.elsevier.com/locate/cej

One-step controllable fabrication of 3D structured self-standing Al_3Ni_2/Ni electrode through molten salt electrolysis for efficient water splitting

Zhongsheng Hua [a,b], Xiaobin Wu [a], Zengli Zhu [a], Jiwen He [a], Shiwei He [a,*], Huan Liu [a,b], Liang Xu [a,b], Yongxiang Yang [a,c], Zhuo Zhao [a,b,*]

[a] School of Metallurgical Engineering, Anhui University of Technology, Maxiang Road, Maanshan 243032, China
[b] Key Laboratory of Metallurgical Emission Reduction & Resources Recycling (Anhui University of Technology), Ministry of Education, Maanshan 243002, China
[c] Department of Materials Science and Engineering, Delft University of Technology, Mekelweg 2, 2628 CD Delft, the Netherlands

ARTICLE INFO

Keywords:
Al_3Ni_2/Ni electrode
Molten salt electrolysis
Water splitting
Electrocatalytic performance
Hydrogen evolution reaction

ABSTRACT

Exploring more efficient and low-cost electrocatalysts to replace platinum (Pt) is highly desired to promote the practical hydrogen production through water splitting. Herein, a facile and effective strategy is proposed to fabricate self-standing Al_3Ni_2/Ni electrode with controlled phase composition and surface morphology, which is obtained by one-step electrochemical reduction of Al^{3+} on commercially available nickel in eutectic NaCl-KCl melt. Different from previously reported approaches, uniform Al_3Ni_2 monolith catalyst can directly grow onto Ni substrate. The deposit possesses unique three-dimensional (3D) cauliflower-like morphology comprising of nano- and microparticles due to the rapid nucleation rate during molten salt electrolysis. The as-fabricated Al_3Ni_2/Ni electrode can be directly used as the cathode to catalyze Hydrogen evolution reaction (HER). Impressively, it exhibits remarkable HER activity comparable to commercial Pt, including a low overpotential of 83.4 mV for a current density of 10 mA cm^{-2}, a small Tafel slope of 40.7 mV dec^{-1}, and excellent long-term stability over 36 h of continuous HER operation in 0.5 M H_2SO_4 solution. The intrinsic catalytic ability of Al_3Ni_2 with the unique hierarchical structure of nano/microsized grains can offer multiple effects, including massive exposed active sites, enhanced charge transfer and mass transport, and fast gas releasing that synergistically contribute to improving the electrocatalytic performance of HER. This work represents a highly promising approach to the design and one-step controllable fabrication of efficient and self-standing base metal electrode for electrocatalytic hydrogen production.

1. Introduction

Nowadays, natural resource and energy have been the focus of common attention around the world. With the continuously increasing demand for energy and gradual exhaustion of fossil fuels, conventional energy production accompanied by environmental problem is getting more and more serious, and thus poses a huge threat to the sustainable development of modern society. Therefore, development of renewable and clean energy sources has become an urgent global issue [1,2]. Hydrogen, a high-quality clean and fully recyclable energy carrier, is considered to be one of the most attractive candidates for the fossil fuels in the future due to its largest energy density [3–5].

Presently, hydrogen is mainly produced from steam reforming of natural gas, petroleum or coal [6], not only still consuming fossil fuels, but also environmentally unfriendly [7,8]. In comparison, electrolytic water splitting is generally regarded as a more sustainable and cleaner approach for hydrogen production [9,10]. Although the technology based on water electrolysis is simple and can be applied to large-scale industrial production, it is underdeveloped and just accounts for approximately 4% of the total hydrogen production because of the fairly high overpotential (-1.48 V) during hydrogen evolution reaction (HER) [11–13]. Currently, the noble metal of platinum remains the only HER catalyst material that can reduce such a large overpotential [14]. Nevertheless, the high cost has restrained its widespread commercial application in water electrolysis [15]. To make the hydrogen fuel produced from water electrolysis economically competitive, it is crucial to explore advanced electrode material, which should not only efficiently catalyze HER at a reasonable overpotential, but also be made from less expensive materials [15–17].

To date, considerable studies have been conducted among

* Corresponding Authors.
E-mail addresses: heshiweiahut@163.com (S. He), zhaozhuo1018@163.com (Z. Zhao).

https://doi.org/10.1016/j.cej.2021.131743
Received 18 April 2021; Received in revised form 25 July 2021; Accepted 6 August 2021
Available online 14 August 2021

researchers all over the world to explore a highly active and earth-abundant HER electrocatalysts [18–21]. Ni-based materials are favorable non-noble metal alternatives for HER catalysts owing to their comparatively high activity and stability [22–27]. It has been reported that the stimulation of diffusion of Al into Ni can effectively enhance the electrocatalytic activity [28], and thereby various Al-Ni alloys have been synthesized as HER catalysts [8,28–31]. In particular, the formation of Al_3Ni_2 intermetallic compound, with large surface roughness and small grain size, in Al-Ni alloys is highly favorable to the catalytic performance [11,28]. Moreover, Al-Ni alloys have also shown admirable acid/alkali corrosion resistance, good oxidation resistance, excellent mechanical properties as well as good electrical conductivity [32–35], which are equally important to the fabricated electrode. In view of these features, Ni-Al alloys with an enrichment of Al_3Ni_2 phase are considered as the promising electrocatalysts for HER.

Since the HER process occurs on the surface of the catalyst, nanostructuring is widely adopted to increase the surface area and thus enhance the catalytic performance. Hence, most of Ni-based electrocatalysts are generally synthesized as powder with various low-dimensional nanostructures [36–38]. The powder catalysts should be attached to a current collector to assemble into an electrode by using agglomerants such as Nafion and polytetrafluoroethylene, which inevitably impedes diffusion and blocks catalytically active sites and subsequently results in high resistance and declined electrocatalytic performance [8,39]. Furthermore, the coated catalysts are prone to peel off from the substrate owing to the poor adhesive force. Nanostructuring of monolith, rather than particles, is a useful way to avoid the above-mentioned issues. Among the techniques for fabricating nanoporous monolith, de-alloying is widely adopted to generate uniform nanoporous structure from an alloy by selective leaching the more reactive element through electro-oxidation [40]. Zhang et al. have reported an effective and compelling in situ construction of Ni-Al catalytic electrode by electrochemical de-alloying of Al-Ni monolith fabricated from pressing - fast sintering of commercial Al-Ni alloy powders [8]. Noteworthily, the de-alloying process coincides with the HER process, and the resulting Al_3Ni_2 phase enriched nanoporous Al-Ni monolith catalyst exhibits low overpotentials of merely −50 mV and −57 mV at the current densities of −10 and −100 mA cm^{-2}, respectively. Zhou et al. have designed a self-standing NiO/Al_3Ni_2 electrode via melt-spinning followed by electrochemical de-alloying [31]. Due to the specific nanostructure and the synergistic effect of NiO and Al_3Ni_2 phase, the fabricated nanoporous catalyst exhibits remarkable HER activity, which is even superior to commercial Pt at high current density. These works confirm that the morphology and phase component of the Al-Ni alloy catalyst are extremely crucial to the HER activity, and should be well controlled during the synthesis process.

Most of the current research concerning Ni-based catalysts is primarily focusing on the electrocatalytic activity toward HER. Nevertheless, the controllable synthesis of catalyst with tailored phase composition and morphology is often not receiving enough attention. Additionally, the synthesis approaches proposed in the current literature still need to be further improved because of either the complicated synthesis steps or the laborious operations. To the best of our knowledge, reports on direct fabrication of a self-supported catalytic electrode are very limited. Therefore, direct in situ synthesis of electrocatalyst on a suitable conductive substrate, namely, facile one-step fabrication of a self-standing and binder-free electrode, is highly desirable.

Molten salt electrolysis, an effective method for the production of both active and non-reactive metals and alloys, has also been verified as a promising approach to fabricate functional materials [41] by controlling the electrochemical reaction process on the well-designed electrode and taking advantage of the enhanced mass transfer and facilitated reaction kinetics in a specific high-temperature electrolyte [42]. Inspired by the outstanding catalytic performance of Al_3Ni_2 [8,31], as well as the successful molten salt electrolytic synthesis of aluminum alloy [43] and value-added functional materials [44,45], herein, we propose, for the first time, a one-step assembly strategy to fabricate Al_3Ni_2 alloy coated Ni (denoted as Al_3Ni_2/Ni) catalytic electrode by electroreduction of Al^{3+} on a conductive nickel current collector in molten salts, which could be directly used as an active cathode for HER. This work is devoted to understanding the reaction mechanism for direct fabrication morphology and phase-controlled Al-Ni alloy catalytic electrode for efficient water splitting. Therefore, the electrochemical reduction behavior of Al^{3+} on nickel was firstly investigated to shed some light on the formation mechanism and the controllable synthesis of Al-Ni alloy with tailored phase composition and surface morphology using molten salt electrolysis. Afterwards, the catalytic performance of the as-fabricated Al_3Ni_2/Ni was explored by directly employing it as the cathode for HER without any further processing. This work affords a new insight into one-step controllable fabrication of novel self-standing Ni-based catalytic electrode for highly efficient water splitting.

2. Experimental section

2.1. Preparation of melt

All reagents used in the experiments were of analytical grade and supplied by Shanghai Aladdin Bio-Chem Technology Co. LTD, China. The mixture of NaCl and KCl with the eutectic composition (50.6:49.4 mol ratio) was used as the supporting electrolyte due to the favorable properties, such as high electrical conductivity, low melting temperature, good thermal and chemical stabilities, relatively wide electrochemical window and low costs [46]. Anhydrous NaCl and KCl were firstly dried at 200 ℃ for more than 48 h to remove the excess moisture, and then melted in a corundum crucible located in an electric furnace at 700 ℃. The temperature of the melt was monitored using a nickel–chromium thermocouple sheathed in an end-closed corundum tube. The melt was pre-electrolyzed at −2.10 V (vs. Ag/AgCl) for several hours to remove the possible metal ions impurities. Anhydrous $AlCl_3$ powder was directly added to molten NaCl-KCl as the source for Al^{3+} ions. The atmosphere inside the electric furnace was maintained to be inert by continuous circulation of high-purity argon.

2.2. Measurements of electrochemical behavior of Al^{3+} on nickel

All electrochemical experiments were carried out in a traditional three-electrode cell using a PARSTAT 2273 electrochemical workstation (Ametek Group Co., American) controlled with the PowerSuite software package. The reference electrode was a home-made Ag/AgCl electrode, which was built with a silver wire (1 mm diameter, 99.99% purity) dipped into the solution of AgCl (2.0 mol%) in eutectic NaCl-KCl melt contained in a mullite tube [47]. All potentials were measured with respect to this Ag^+/Ag couple in this study. The working electrode was either a tungsten wire (1 mm diameter, 99.99% purity) or a nickel wire (1 mm diameter, 99.99% purity), depending on the electrochemical investigation. The working electrodes were polished and cleaned thoroughly before use. A spectral pure graphite rod (6 mm diameter) was employed as the counter electrode. The active electrode surface area was determined by measuring its immersion depth in the melt after each experiment. Transient electrochemical techniques, including cyclic voltammetry, square wave voltammetry and open circuit chronopotentiometry, were used to investigate the electrochemical reduction of Al^{3+} ions on the solid nickel.

2.3. Preparation and characterization of Al-Ni alloy samples

Al-Ni alloy samples were prepared by potentiostatic electrolysis at different potentials in molten NaCl-KCl-$AlCl_3$ on nickel plates (10 × 40 × 0.3 mm) at 700 ℃. After electrolysis, the samples were initially washed in deionized water and then ultrasonically cleaned in ethanol (99.5% purity) to remove the attached salts on the surface of the alloy

deposit. The phase composition of the deposit was identified with X-ray diffraction (XRD, D8 Advance, Bruker) using a Cu Kα monochrome radiation at 30 kV and 10 mA. The morphology and element distribution of the deposit were characterized by scanning electron microscopy (SEM, SSX-550, Shinadzu) and energy dispersion spectroscopy (EDS) equipped with SEM, respectively. The inner structure was observed by transmission electron microscopy (TEM, FEI Talos F200X, Thermo Fischer) and high-resolution TEM (HRTEM). The elemental composition and valence state were analyzed through X-ray photoelectron spectroscopy (XPS, Escalab 250Xi, Thermo Fischer) using an Al Ka radiation excitation source.

2.4. Fabrication of catalytic electrode and electrocatalytic experiments

The catalytic electrode was fabricated by one-step electrochemical deposition of Al-Ni alloy on a nickel wire of 1 mm diameter or a nickel plate of 0.3 mm thickness. The electrocatalytic experiments were conducted on the PARSTAT 2273 electrochemical workstation with a typical three-electrode system in 0.5 M H_2SO_4 electrolyte at room temperature. The as-fabricated electrode with an exposed area of 0.322 cm^2 was employed as the working electrode. A graphite plate and saturated mercuric sulfate electrode (MSE) served as the counter and reference electrodes, respectively. All potentials measured were then calibrated to the reversible hydrogen electrode (RHE) by adding a value of (0.68 + 0.059 pH) V. Linear sweep voltammetry (LSV) was measured in 0.5 M H_2SO_4 solution with a scan rate of 5 mV s^{-1}. Electrochemical impedance spectroscopy (EIS) measurements were carried out at −0.755 V (vs. MSE) in the frequency range of 10^4 Hz to 0.01 Hz with an applied AC voltage of 10 mV. An iR correction to polarization curves and corresponding Tafel plots was made based on the ohmic resistance of the electrolyte measured with EIS. The stability of the as-fabricated Al-Ni alloy catalytic electrode was evaluated by galvanostatic technique with an applied current density of 10 mA cm^{-2} for 36 h. For comparison, the electrocatalytic performance of commercial Pt wire, Ni wire and Al wire with an effective area of 0.322 cm^2 was also examined under the identical conditions.

3. Results and discussion

3.1. Electrochemical behavior of Al^{3+} on nickel

To determine the electrochemical window and compare with the nickel electrode, cyclic voltammetry measurements were firstly conducted on an inert tungsten electrode in the purified eutectic NaCl-KCl melt before and after the addition of $AlCl_3$, as shown in Fig. 1a. From the blue dotted line, representing the typical cyclic voltammogram of blank NaCl-KCl melt, the sharp cathodic signal A starting at −2.20 V (vs. Ag/AgCl) is attributed to the electrochemical reduction of Na^+ to Na,

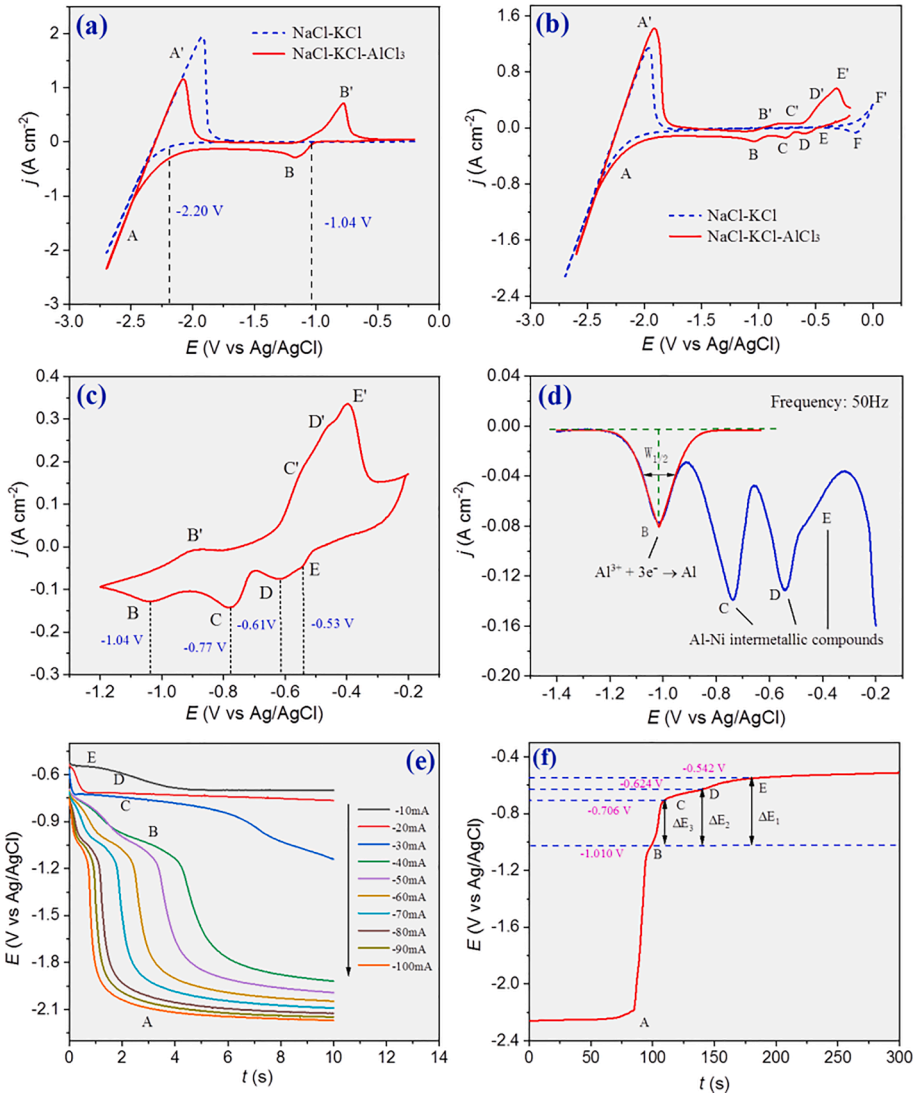

Fig. 1. Cyclic voltammograms measured on tungsten electrode (a) and nickel electrode (b) in NaCl-KCl eutectic melt before (blue dotted line) and after (red solid line) the addition of 0.5 mol% $AlCl_3$; (c) Cyclic voltammogram in the scan range of −0.20 ~ -1.20 V attained on nickel electrode in molten NaCl-KCl-$AlCl_3$(0.5 mol%). Electrode area: 0.322 cm^{-2}, temperature: 700 ℃, scan rate: 0.1 V s^{-1}. (d) Square wave voltammogram attained in the NaCl-KCl-$AlCl_3$ (0.5 mol%) melt at 700 ℃ on nickel electrode (S = 0.322 cm^2). Frequency: 50 Hz, potential step: 1 mV. (e) Chronopotentiograms measured at different current intensities on nickel electrode (S = 0.322 cm^2) in the NaCl-KCl-$AlCl_3$(0.5 mol%) melt at 700 ℃. (f) Open circuit chronopotentiogram attained on nickel electrode (S = 0.322 cm^2) after electrolysis at −2.60 V for 60 s in the NaCl-KCl-$AlCl_3$(0.5 mol%) melt at 700 ℃.

and the anodic signal A′ in the reverse scan is ascribed to the subsequent oxidation of deposited Na metal. No other electrochemical processes present in the explored electrochemical window, verifying that molten NaCl-KCl is applicable for the investigation. After the addition of 0.5 mol % $AlCl_3$, a new couple of redox peaks are detected, as shown by the red solid line. The reduction peak B, at approximately −1.10 V, and the corresponding oxidation peak B′ should be attributed to the deposition of aluminum metal and its subsequent dissolution reaction, respectively. Remarkably, the anodic current shows a much higher amplitude than the cathodic current due to the availability of deposited metal for the stripping [48]. Except for the two couples of redox signals A/A′ and B/B′, no other additional redox peaks have been detected in the voltammogram. Accordingly, it can be inferred that the electrochemical reduction of Al^{3+} to aluminum metal on a tungsten electrode proceeds via a single step in molten NaCl-KCl.

Then, cyclic voltammetry measurements on the nickel electrode were performed in eutectic NaCl-KCl melt at 700 ℃, and the results are shown in Fig. 1b-c. It can be seen from the blue dotted line in Fig. 1b that, aside from the redox signals A/A′ mentioned above, a pair of redox peaks F/F′ present at around −0.10/0 V, which should be caused by the oxidation of nickel electrode [49]. To avoid the dissolution of nickel electrode and further clearly explore the electrochemical behavior of Al^{3+} on solid nickel, the potential terminal for positive sweep is adjusted negative than −0.10 V in subsequent electrochemical investigations. Different from the inert tungsten electrode, nickel electrode reacts with aluminum during its reduction and forms various phases of Al-Ni alloys. Therefore, the shape of the voltammograms measured on nickel electrode is expected to be distinguished from those recorded on an inert one. As illustrated by the red solid curve in Fig. 1b, a small cathodic peak B at around −1.06 V and the not very noticeable anodic peak B′ are ascribed to Al^{3+}/Al redox couple. Meanwhile, a series of new redox signals appearing at more positive potentials than that for the deposition/dissolution of aluminum metal should be associated with the formation/dissolution of different Al-Ni intermetallic compounds. The shift of Al^{3+} reduction potential toward positive values, the so-called underpotential deposition, is attributed to the decrease of the activity of the electrodeposited aluminum metal on an active electrode, due to the formation of various Al-Ni intermetallic compounds.

$$x\mathrm{Al}^{3+} + y\mathrm{Ni} + 3x\mathrm{e}^{-} = \mathrm{Al}_x\mathrm{Ni}_y \quad (1)$$

The equilibrium potential of the system Al^{3+}/Al_xNi_y, E_{Al^{3+}/Al_xNi_y}, can be expressed by the following equation:

$$E_{\mathrm{Al}^{3+}/\mathrm{Al}_x\mathrm{Ni}_y} = E_{\mathrm{Al}^{3+}/\mathrm{Al}} - \frac{RT}{nF}\ln\left[a_{\mathrm{Al}}\left(\text{in } \mathrm{Al}_x\mathrm{Ni}_y\right)\right] \quad (2)$$

where $E_{Al^{3+}/Al}$denotes the equilibrium potential of pure Al element, R is the universal gas constant (8.314 J mol^{-1} K^{-1}), T represents the absolute temperature (K), n corresponds to the number of electrons exchanged, F is the Faraday constant (96,485C mol^{-1}), and a_{Al}(in Al_xNi_y) designates the activity of Al in the intermetallic compound Al_xNi_y. Since the activity of aluminum in Al_xNi_y intermetallic is less than unity, thus.

However, these redox peaks are overlapped in the current background and not well defined. To assign the attribution of these redox peaks, the reduction behavior of Al^{3+} ions on the nickel electrode was subsequently investigated by cyclic voltammetry at the reversion potential of −1.20 V in eutectic NaCl-KCl melt. As shown in Fig. 1c, except for the signals B/B′, three pairs of redox peaks C/C′, D/D′ and E/E′, caused by the formation of various Al-Ni intermetallics are clearly observed. The values of redox peak potentials are listed in Table S1. According to the binary phase diagram of Al-Ni system [49], aluminum can form four intermetallic compounds with nickel such as Al_3Ni, Al_3Ni_2, AlNi and $AlNi_3$, at the temperature of the experiments. Nevertheless, only three pairs of peaks corresponding to the formation and dissolution of Al-Ni intermetallic compounds, respectively, present in the voltammogram. These three Al-Ni intermetallics are considered to be Al_3Ni_2, AlNi and $AlNi_3$, respectively. The absence of intermetallic Al_3Ni could be ascribed to the very slow formation rate of the Al-richer phase on the nickel substrate kinetically, resulted from the intermetallic diffusion limitations. Similar phenomena have also been reported in other studies investigating the electrochemical formation of Y-Al [43], Mg-Nd [46] and Mg-Tm [50] alloys by cyclic voltammograms on both inert and active electrodes.

Since cathodic peaks, D and E, are very close and overlap each other, their cathodic peak potentials cannot be clearly confirmed from cyclic voltammograms. Hence, square wave voltammetry, a more sensitive transient electrochemical technique than cyclic voltammetry, was employed to further clarify the reduction behavior of Al^{3+} on nickel electrode. Fig. 1d represents the square wave voltammogram of NaCl-KCl-$AlCl_3$ (0.5 mol%) system on nickel electrode at 700 ℃ with the signal frequency of 50 Hz and step potential of 1 mV. Four peaks appear in the voltammogram scanning from −0.20 to −1.40 V. Peak B, at approximately −1.02 V, is obviously attributed to the electrochemical reduction of Al^{3+}. In the case of a reversible soluble - insoluble electrochemical system at low frequency, the number of exchanged electrons in the electrochemical reaction can be calculated from the following equation by measuring the half-width of the peak ($W_{1/2}$) [51].

$$W_{1/2} = \frac{3.52RT}{nF} \quad (3)$$

The value of n is calculated to be 2.6, and approximate to 3, confirming that peak B corresponds to the redox couple of Al^{3+}/Al. Peaks C, D and E should be associated with the formation of different Al-Ni intermetallic compounds, respectively. Peak E appears as a shoulder prior to peak D, because its potential value is very close to that of peak D. A similar behavior has also been detected by Wang et al. in their investigation of Mg-Ni alloy by square wave voltammetry [52]. Based on the square wave voltammetry, the potential values of these four reduction peaks are confirmed, as presented in Table S1.

Chronopotentiometry was also carried out to further investigate the reduction process of Al^{3+} on nickel. Fig. 1e depicts the typical chronopotentiogram obtained on nickel electrode in NaCl-KCl-$AlCl_3$(0.5 mol %) melt at 700 ℃ with various current densities. Five potential plateaus present in the graph. When the applied current is −10 mA, three plateaus, E, D and C, are observed. According to the electrochemical reduction process investigated in Fig. 1b-d, three signals corresponding to the formation of Al-Ni alloys are present between −0.40 ~ -0.80 V. Therefore, these three plateaus should be related with the formation of various Al-Ni intermetallic compounds. Moreover, plateau E at the beginning of the curve is very close to plateau D. This phenomenon is also consistent with those observed from cyclic voltammogram and square wave voltammogram. When the current increases to −40 mA, the fourth plateau (plateau B) appears at approximately −1.0 V, which corresponds to the reduction of Al^{3+}. With further increasing the applied current, there is a sharp decline in the potential, and the potential gradually approaches to a limited value at around −2.20 V (plateau A), implying that massive Na^+ starts to be reduced to metallic sodium. The plateau potentials obtained from chronopotentiogram are also listed in Table S1, which accord closely with those attained from cyclic voltammogram and square wave voltammogram.

Different from the aforementioned transient electrochemical techniques, open circuit chronopotentiometry is unaffected by the nuclear overpotential, and is more appreciate for determining the equilibrium potential of the system. As shown in Fig. 1b-c, the anodic peaks associated with the dissolution of Al-Ni alloys were not evident in cyclic voltammograms, and thus open circuit chronopotentiometry was performed to further explore the underlying formation and dissolution process. Firstly, potentiostatic electrolysis was conducted for a short period to form a thin layer specimen on the electrode, and then the open circuit potential of the electrode was registered as a function of time. Since the deposited aluminum metal reacts with nickel and diffuses into

the nickel electrode generating Al-Ni alloys, the electrode potential will shift to more positive values. Consequently, a potential plateau representing the co-existence of two phases on the surface of the electrode can be observed [53].

Fig. 1f illustrates the open circuit transient curve measured on nickel electrode after electrolysis at −2.60 V in the NaCl-KCl-$AlCl_3$(0.5 mol%) melt at 700 ℃ for 60 s. Five potential plateaus can be clearly identified, and equilibrium potentials, representing the dissolution of the deposit, are presented in Table S1. The first plateau staying at −2.25 V (plateau A) is undoubtedly related to the presence of metallic sodium and corresponds to equilibrium reaction of Na^+/Na. The second plateau at around −1.01 V (plateau B) should be ascribed to the re-oxidation of the deposited aluminum metal on the surface of the electrode and correlated with the Al^{3+}/Al redox couple. Afterward, three plateaus C, D and E, appearing successively in the chronopotentiogram, are associated with the two-phase coexisting states of various Al-Ni intermetallic compounds. The higher the Al content is in the intermetallic compound Al_xNi_y, the closer the equilibrium potential of Al_xNi_y is to that of Al metal in the chronopotentiogram [54,55]. According to the subsequent XRD and SEM-EDS analyses of the alloys prepared by potentiostatic electrolysis, plateaus C, D and E should be involved in the coexisting states of Al_3Ni_2, AlNi and $AlNi_3$, respectively. Therefore, the five potential plateaus in Fig. 1f correlated equilibrium reactions could be described as follows:

Plateau C

$$Al^{3+} + 2AlNi + 3e^- \leftrightarrow 3AlNi_{2/3} \quad (4)$$

Plateau D

$$Al^{3+} + \frac{1}{2}AlNi_3 + 3e^- \leftrightarrow \frac{3}{2}AlNi \quad (5)$$

Plateau E

$$Al^{3+} + 3Ni + 3e^- \leftrightarrow AlNi_3 \quad (6)$$

3.2. Thermodynamic properties of Al-Ni intermetallic compounds

According to the open circuit chronopotentiogram in Fig. 1f, the equilibrium potential of the two-phase coexisting state of Al-Ni alloys, referenced to the Ag^+/Ag couple, can be converted to the electromotive force (emf) ΔE by measuring the potential against Al, as listed in Table 1. In this way, the corresponding relative partial molar Gibbs free energy of Al, $\Delta\overline{G}_{Al}$, in the two-phase coexisting Al-Ni alloys can be calculated from the emf by the following expression:

$$\Delta\overline{G}_{Al} = -3F\Delta E \quad (7)$$

Additionally, when the electrode surface is within a coexistence of alloys of definite chemical compositions $Al_{x1}Ni$ and $Al_{x2}Ni$, the activity of Al is fixed by the following equilibrium reaction:

$$Al_{x1}Ni + (x_2 - x_1)Al^{3+} + 3(x_2 - x_1)e^- \rightarrow Al_{x2}Ni \quad (8)$$

and the emf will stay constant during the full transformation of the specific alloy $Al_{x1}Ni$ into the alloy $Al_{x2}Ni$. Therefore, the activity of Al in various Al-Ni intermetallic compounds can be estimated based on the obtained emf by the following equation:

$$\Delta E = -\frac{RT}{3F}ln(a_{Al}(\text{in } Al_xNi_y)) \quad (9)$$

The calculated thermodynamic data of various Al-Ni intermetallic compounds are summarized in Table 1. The magnitude of activities for Al in Al-Ni intermetallic compounds are found to vary from the order of 10^{-8} to 10^{-5}. The Al activity increases when aluminum becomes more prevalent in the two-phase coexisting state. For example, the presence of Al_3Ni_2 is conducive to enhancing the Al activity in the coexisting phases. It is generally accepted that Al atoms can affect the electronic structure of Al − Ni catalyst and surface adsorption energy of the reactants [56]. Thereby, upon doping Al element to form an Al-rich phase of Al_3Ni_2 intermetallic, Ni atoms are expected to gain additional electrons readily from adjacent Al atoms, leading to the optimal interaction between Ni active sites and reactant molecules.

Moreover, on the basis of the equilibrium reactions, the standard molar Gibbs energy of formation (ΔG_f^o (kJ mol^{-1})) of the intermetallic compound $Al_{x2}Ni$ is related to that of $Al_{x1}Ni$, and can be formulated as follows [57]:

$$\Delta G_f^o(Al_{x2}Ni) = -3F\int_{x1}^{x2}\Delta E(x)dx + \Delta G_f^o(Al_{x1}Ni) \quad (10)$$

The calculated values are summarized in Table S2. It can be seen that compared with the intermetallics $AlNi_3$ and AlNi, the formation of intermetallic $AlNi_{2/3}$ is somewhat more difficult thermodynamically, although it is likely more favorable for the catalytic activity toward HER. So, a larger emf, that is a more negative potential, is required to obtain the Al-rich intermetallic Al_3Ni_2 via electroreduction of Al^{3+} on nickel.

Table 1
Thermodynamic properties of Al for Al-Ni intermetallic compounds in the two-phase coexisting states.

Plateau	E/V (vs. Ag/AgCl)	ΔE/V (vs. Al^{3+}/Al)	$\Delta\overline{G}_{Al}$/(kJ·(mol Al)$^{-1}$)	a_{Al}
B	−1.010 ± 0.005	–	–	–
C	−0.706 ± 0.003	0.304 ± 0.008	−87.99 ± 2.32	1.89×10^{-5}
D	−0.624 ± 0.002	0.386 ± 0.007	−111.73 ± 2.03	1.00×10^{-6}
E	−0.542 ± 0.001	0.468 ± 0.006	−135.46 ± 1.74	5.34×10^{-8}

3.3. Electrodeposition and characterization of Al–Ni alloys

It is widely acknowledged that potentiostatic electrolysis has the superiority in controlling the phase composition of the alloys produced. In order to characterize the deposited alloys and to associate the phase composition of the deposit with the deposition potential, Al-Ni alloy samples were prepared by potentiostatic electrolysis in molten NaCl-KCl-$AlCl_3$(1.5 mol%) using rectangular nickel plates as the working electrodes at different potentials for the periods ranging from 5 to 7 h. Fig. 2a depicts the XRD patterns of the deposits obtained on nickel electrode at 700 ℃. When electrolysis was conducted at −1.0 V (vs. Ag/AgCl) for 7 h, metallic Ni and intermetallic compounds of AlNi and $AlNi_3$ were detected in the sample. The Ni phase should be originated from nickel substrate. It can thus be inferred that a mixture of Al-Ni alloys was formed on nickel electrode after electrolysis at −1.0 V for 7 h. At the applied potential of −1.1 V, the AlNi phase emerged as the predominant phase, and meanwhile a new phase of Al_3Ni_2 formed in the deposit. When electrolysis was conducted at a more negative potential of −1.2 V, the deposit was identified as Al_3Ni_2 and $AlNi_3$ phases, but Al_3Ni_2 was overwhelmingly predominant. It is noteworthy that the impurity $KAlO_2$, caused by the hydrolysis and dehydration reaction of residual chlorides on the sample, was found as a minor phase in Fig. 2a. The phase transformation of the deposit (see Table S3) indicates that the Al content in the obtained alloys increases with the negative shift of applied potential, that is, more negative electrolysis potential is in favor of the formation of Al rich phase. Especially, pure Al phase was not found in the deposits, although the applied potential is negative than the deposition potential of Al metal. It signifies that the deposited Al can continuously react with a certain amount of the Al-Ni alloy previously generated on the surface nickel electrode to form a more aluminum rich alloy. Similar behavior has also been reported by Luo et al. [58] in electrochemical preparation of Nd-Zn alloys. In addition, broad diffraction peaks were present in the XRD patterns, suggesting that Al-Ni alloys with fine grain would be produced on nickel electrode by

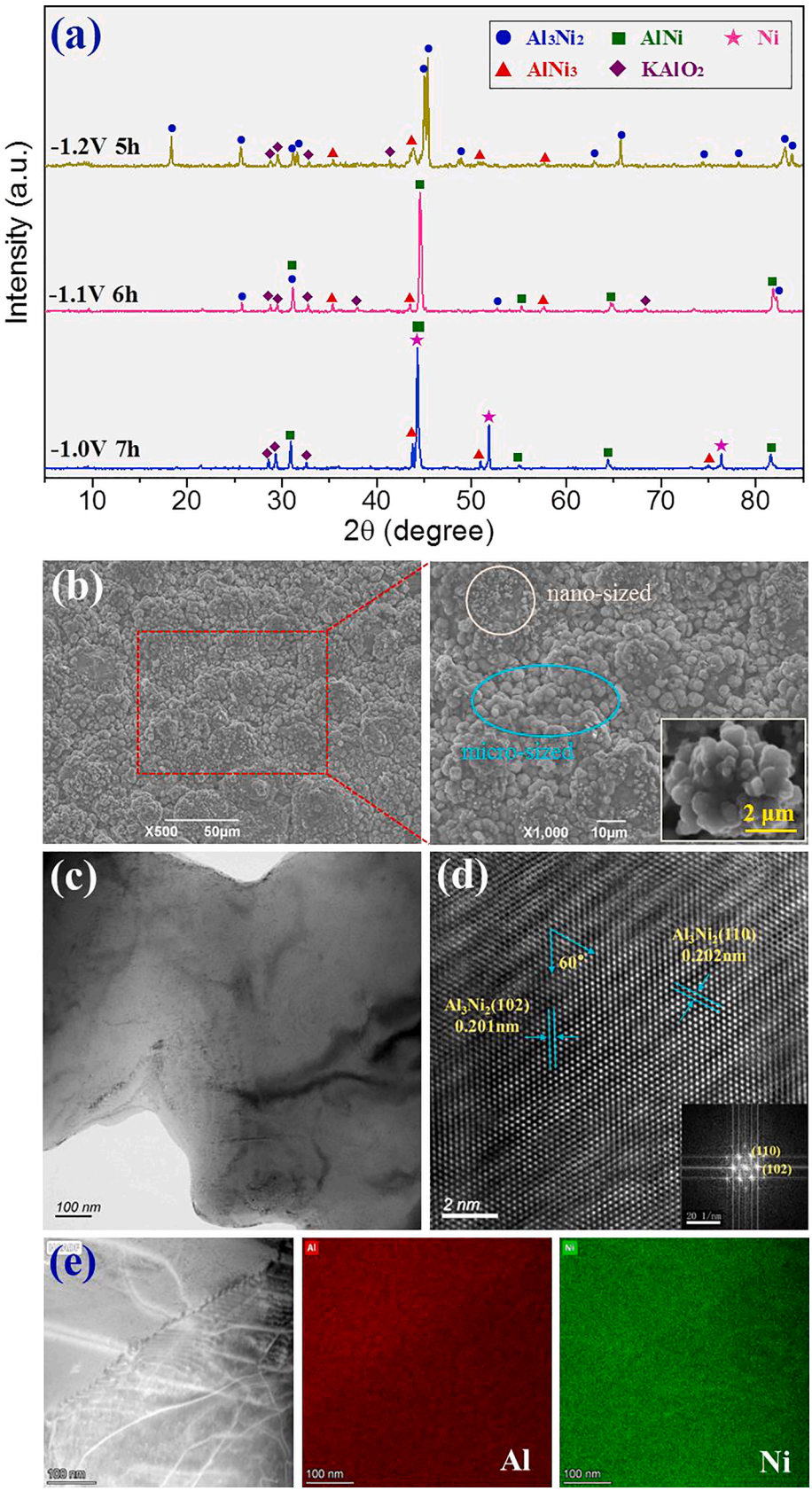

Fig. 2. (a) XRD patterns of the deposits obtained on nickel plate in molten NaCl-KCl-$AlCl_3$(1.5 mol%) by potentiostatic electrolysis at 700 ℃. (b) Surface morphology, (c) TEM, (d) HRTEM and (e) HAADF-STEM and corresponding EDS mapping images of Al_3Ni_2/Ni sample fabricated by potentiostatic electrolysis at −1.2 V for 5 h. Inset in (b) shows the high resolution SEM image, and inset in (d) is the corresponding FFT patterns.

potentiostatic electrolysis in the NaCl-KCl-$AlCl_3$ melt.

According to the electrolysis experiments, the phase compositions of the deposit on nickel substrate can be adjusted by controlling the applied potential. As mentioned above, the Al_3Ni_2 intermetallic demonstrates good physicochemical properties and high catalytic activity for water splitting. Herein, potentiostatic electrolysis was performed on nickel substrate at −1.2 V for 5 h to fabricate the Al_3Ni_2/Ni electrode, which could be directly employed as the cathode for hydrogen production. The SEM image of the surface morphology of the fabricated Al_3Ni_2/Ni electrode was shown in Fig. 2b. Electrochemical deposition of Al-Ni alloy on nickel endows its surface numerous particles with grain size ranging from tens of nanometers to several micrometers. This could be attributed to the competitive advantage of molten salt electrolysis over other technologies. Since the electrolysis proceeds at a high temperature of 700 ℃, the nucleation of Al-Ni alloy via electro-reduction of Al^{3+} on nickel is extremely fast, while the driving force for grain growth is comparatively insufficient, resulting in the formation of nanocrystal or microcrystal structure of Al_3Ni_2 phase. The generated Al_3Ni_2 grains with very limited sizes grow into 3D cauliflower-like particles and densely distribute on the surface of the electrode. High-resolution SEM image (inset in Fig. 2b) shows that the macroparticles on Al_3Ni_2/Ni surface are composed of stacked microparticles with interconnected and open pores among them. The above coarsening structures provide a tremendous number of active sites for HER and enhance their contact with electrolyte, thus expectedly serving as an efficient catalyst for water splitting.

For further elucidating the microstructure and exact crystal phase of the fabricated Al_3Ni_2/Ni sample, the alloy deposit on nickel substrate was thinned for TEM analysis, as shown in Fig. 2c-d. The HRTEM image (Fig. 2d) reveals that the main phase composition of the deposit is Al_3Ni_2 crystal, as evidenced by the clear lattice fringes with the measured crystal interplanar distances of about 0.201 and 0.202 nm showing a crystal angle of 60°, which can be assigned to the (1 0 2) and (1 1 0) planes of hexagonal Al_3Ni_2, respectively. The corresponding Fast Fourier transform (FFT) pattern (inset of Fig. 2d) taken from the HRTEM image shows a well-defined spotted electron diffraction pattern, further confirming the single-crystalline nature of the Al_3Ni_2 crystals. High-angle annular dark field scanning transmission electron microscopy (HAADF-STEM) and corresponding EDS elemental mapping images (Fig. 2e) illustrate the homogeneous spatial distribution of Al and Ni in the deposit. The Al_3Ni_2(1 1 0) plane is the most stable facet during the HER process, and the Al_3Ni_2 intermetallic with the well-defined crystal structure and atomic position will possess high stability because the ordering effect can effectively impede particular element dissolving [31]. Additionally, the periodic structure of the crystal could essentially isolate the Ni atoms in the ordered Al_3Ni_2 intermetallic which act as the active sites for HER, and thus ensures the homogeneous distribution of active sites on the catalyst.

XPS study was employed to investigate the surface characteristics of Al_3Ni_2/Ni since the electrocatalytic activity for HER is sensitive to the chemical state of the catalyst in the surface layer. The XPS survey spectrum of the as-fabricated Al_3Ni_2/Ni sample shown in Fig. 3a illustrates that the deposited film comprises Al, Ni and O elements based on the specific binding energy values calibrated by the C 1 s peak (284.60 eV). The element O likely derives from the minor surface oxidation of Al-Ni alloy and adsorbed oxygen-containing species of O_2, CO_2 or H_2O. The Ni 2p spectrum of Al_3Ni_2/Ni (Fig. 3b) shows two distinct peaks at about 852.6 and 869.7 eV, which can be assigned to the binding energy of spin–orbit doublet Ni $2p_{3/2}$ and Ni $2p_{1/2}$ for metallic Ni [59]. Besides, two main peaks located at 856.1 and 873.7 eV with two shake-up satellite peaks at 861.9 and 879.9 eV correspond to the energy level of Ni

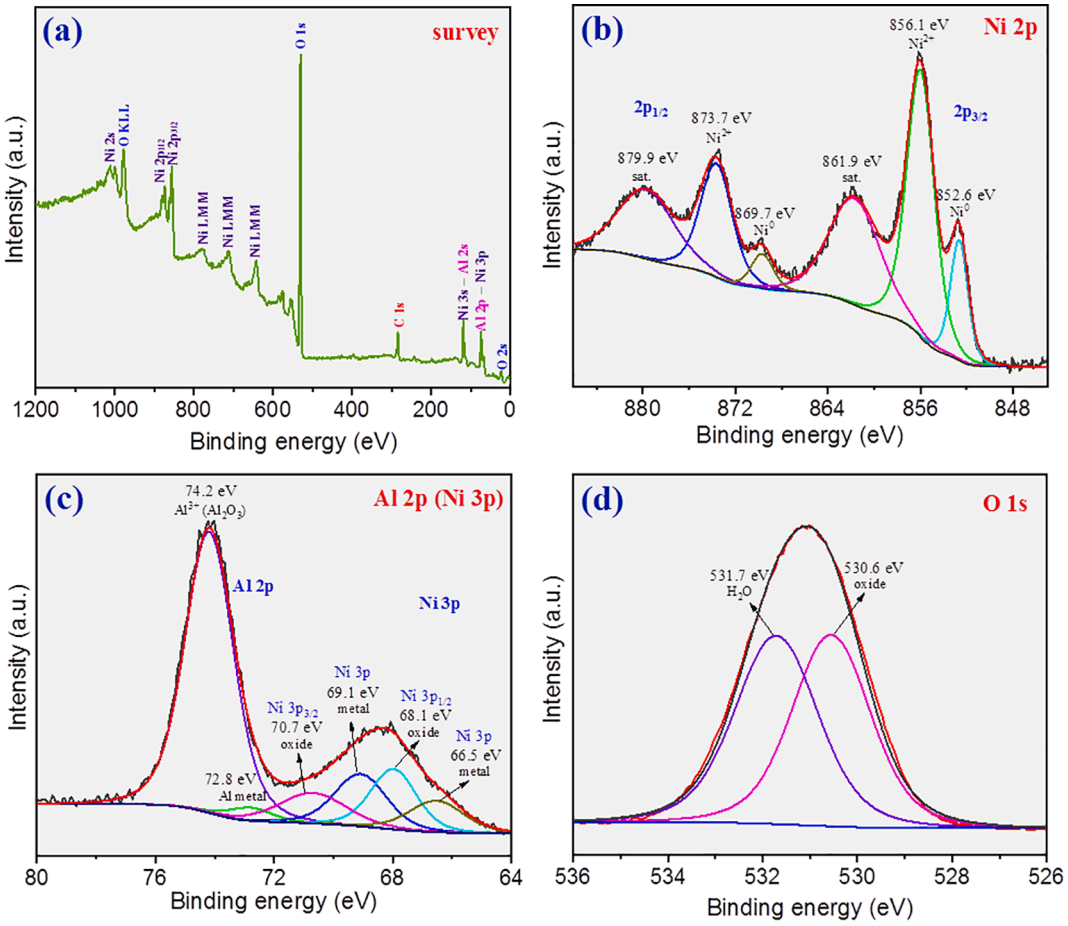

Fig. 3. XPS spectra of Al_3Ni_2/Ni electrode: (a) survey, (b) Ni 2p, (c) Al 2p (Ni 3p) and (d) O 1 s.

$2p_{3/2}$ and Ni $2p_{1/2}$ of Ni^{2+} valence states [60], probably arising from the surface oxidation of Al-Ni alloys. Expectedly, the oxidative and metallic Ni also present in the Ni 3p spectrum (Fig. 3c). The Al 2p spectrum (Fig. 3c) can be deconvoluted into two peaks at 72.8 and 74.2 eV, representing metallic Al and Al^{3+} in Al_2O_3, respectively [31,61]. The Al 2p peak at 72.8 eV along with the Ni $2p_{3/2}$ at 852.6 eV and Ni $2p_{1/2}$ at 869.7 eV manifests the coupling of Al and Ni atoms, and further confirms the existence of Al_3Ni_2 intermetallic in the deposit. It can also be inferred that nickel and aluminum oxide passive film can generate on the surface of the Al_3Ni_2/Ni electrode, thus protecting the electrode from acid attack. For O 1 s spectrum (Fig. 3d), the binding energy peaks positioned at 530.6 and 531.7 eV can be ascribed to the characteristic of chemical state of O^{2-} in oxides [62] and surface adsorbed H_2O molecules [31], respectively. Since the HER takes place on the surface of the electrode, the H_2O adsorption on the electrode is consequentially crucial for the electrocatalytic water splitting. In this regard, faster charge transfer from the Al_3Ni_2 catalyst surface to H_2O molecules could occur during the HER process, and the adsorption of H_2O on the Al_3Ni_2/Ni electrode would be energetically favored, thus facilitating the water splitting.

3.4. *Preliminary discussions on formation mechanism of Al_3Ni_2/Ni electrode*

Fig. 4a-b displays the back-scattering SEM images of the cross section of the samples obtained under potentiostatic electrolysis at −1.0 for 7 h and −1.2 V for 5 h, respectively. As seen from Fig. 4a that a thin film of approximately 10 μm was formed on the nickel electrode, since the average electrolytic current was very low when electrolysis at −1.0 V. The alloy film was composed of two layers, and the EDS quantitative analysis indicates the molar ratios of Al/Ni for the superficial and inner layer are around 1:1 and 1:3 (Fig. S1), corresponding to AlNi and $AlNi_3$, respectively. The formation of the aluminum-poor phase of $AlNi_3$ intermetallic in the deposit was also confirmed by the crystal facets for $AlNi_3$(1 1 2) accompanied by the FFT patterns and the corresponding EDS result (Fig. S2). When electrolysis was performed at a more negative potential of −1.2 V, a uniform deposit with a dense state attached tightly on the nickel matrix was observed in Fig. 4b. EDS results (Fig. S1 and Fig. S3) indicate that the molar content of Al is nearly 1.5 times as that of Ni, confirming that the deposit is mainly composed of the intermetallic compound Al_3Ni_2. Obviously, the deposit acquired at −1.2 V is much thicker than that obtained at −1.0 V, verifying the significance of nucleation overpotential, to a certain extent, for the formation and growth of Al-Ni alloys onto nickel substrate. It can also be clearly seen from Fig. 4b that the thickness of nickel plate decreases due to its alloying reaction with deposited aluminum. Nevertheless, the whole electrode thickened after electrolysis because of the volume expansion during alloy formation [63]. Particularly, a distinguishing feature of the adopted molten salt electrolysis technology is that the generated Al_3Ni_2 alloy is in the solid state, effectively restraining the element segregation which occurs inevitably in traditional technologies, such as high-temperature melting, and powder metallurgy via diffusion alloying. As shown in Fig. S4, the uniform luster of element mapping further confirms the homogeneous distribution of Al and Ni in the sample gained at −1.2 V for 5 h, which is beneficial to the improvement of its catalytic

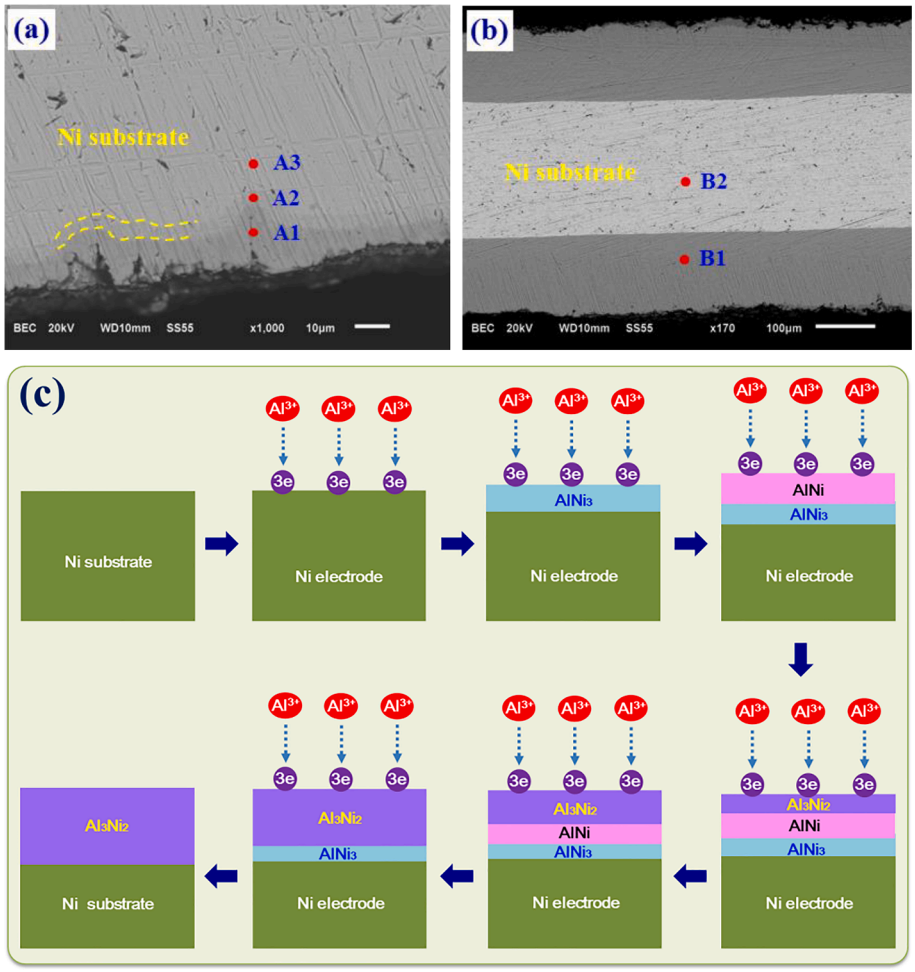

Fig. 4. SEM images of the cross section of the samples obtained from molten NaCl-KCl-$AlCl_3$(1.5 mol%) at 700 ℃ by potentiostatic electrolysis on nickel at (a) −1.0 V for 7 h and (b) −1.2 V for 5 h. (c) Schematic illustration of the possible formation mechanism of Al-Ni alloy deposit on nickel.

performances.

On the basis of aforementioned discussions, an illustration of the possible formation mechanism of Al-Ni alloys on nickel is suggested in Fig. 4c. As the potentiostatic electrolysis begins, the Al^{3+} ions in NaCl-KCl melt are reduced directly into Al-Ni alloy due to the under-potential deposition on the reactive nickel electrode. After a period of electrolysis, a thin film of aluminum-poor phase of $AlNi_3$ is formed on nickel substrate. Subsequently, the Al^{3+} ions will then be reduced and diffuse into the preferentially deposited Al-Ni alloy to form the new aluminum-rich phases AlNi and Al_3Ni_2, successively. With the electrolysis progressing, the reduced aluminum continuously transfers into the Al-Ni alloy film, and consequently more aluminum rich phase such as Al_3Ni_2, is getting more and more prominent in the deposit. During the alloy formation process, the applied potential is of great importance to the phase composition of the deposit obtained by potentiostatic electrolysis. Firstly, due to the nucleation overpotential in alloy formation, more negative potential is propitious to the reduction of Al^{3+} into Al-Ni alloys. Secondly, the more negative potential is applied, the larger the electrolytic current is, and thus the more alloys will be deposited. Therefore, a thin film identified as the mixture of AlNi and $AlNi_3$ intermetallic compounds was deposited on nickel substrate by electrolysis at −1.0 V for 7 h. However, a much thicker film mainly composed of aluminum-rich phase of Al_3Ni_2 was obtained when electrolysis at −1.2 V even for a shorter time of 5 h. Accordingly, to acquire the most aluminum rich Al-Ni alloy deposit, the potential applied for potentiostatic electrolysis should be more negative than −1.2 V.

3.5. Electrocatalytic performance of Al_3Ni_2/Ni electrode for HER

The electrocatalytic activity of the fabricated Al_3Ni_2/Ni electrode for HER was assessed in 0.5 M H_2SO_4 solution by directly adopting it as the working electrode. LSV curves measured at a low scan rate can be regarded as steady-state responses as polarization curves. Fig. 5a depicts the typical polarization curve of Al_3Ni_2/Ni electrode, along with those of commercial Pt, Al and Ni under the identical conditions as references. As expected, the Al_3Ni_2/Ni electrode exhibits a very comparable HER activity to Pt (Table S4), with current density increasing rapidly along the increasing overpotential, which is very advantageous for its practical application in water splitting. As shown in Fig. 5b, the overpotential at 10 mA cm^{-2} (η_{10}) of the Al_3Ni_2/Ni electrode, a valid parameter to evaluate the electrocatalytic performance, is just 83.4 mV, significantly outperforming nickel (346.6 mV) and aluminum (634.2 mV). For comparison, the overpotential at specific current density of 1 mA cm^{-2} (η_{onset}), 10 mA cm^{-2} (η_{10}) and 100 mA cm^{-2} (η_{100}) of recently reported state-of-art Ni-based catalysts are collected (Table S5), displaying that the as-fabricated Al_3Ni_2/Ni electrode exhibits superior electrocatalytic activity for hydrogen evolution. It is to be noted that in the negative scan from 0 to −0.05 V, an anodic current appears in the LSV curve of the Al_3Ni_2/Ni sample. Pure Al and Ni are highly corrosion resistant to sulfuric acid solution due to the formation of compact passive oxide film [64,65]. However, the Al_3Ni_2/Ni electrode with rough surface has a slightly lower pitting potential because of the heterogeneous distribution of nickel and aluminum oxides in the passive film [66], and thus may be attacked by the electrolyte before the oxide passive film has been compactly formed on its surface. Considering the standard electrode potentials (Fig. S5) and the system compositions, the observed anodic current is thus related to the slight dissolution or the oxidation of Al, as reported by Han et al. [67] and Zhang et al. [8].

In order to gain the kinetic insights into the HER pathway and catalytic activity, the Tafel plots were derived from the polarization curves

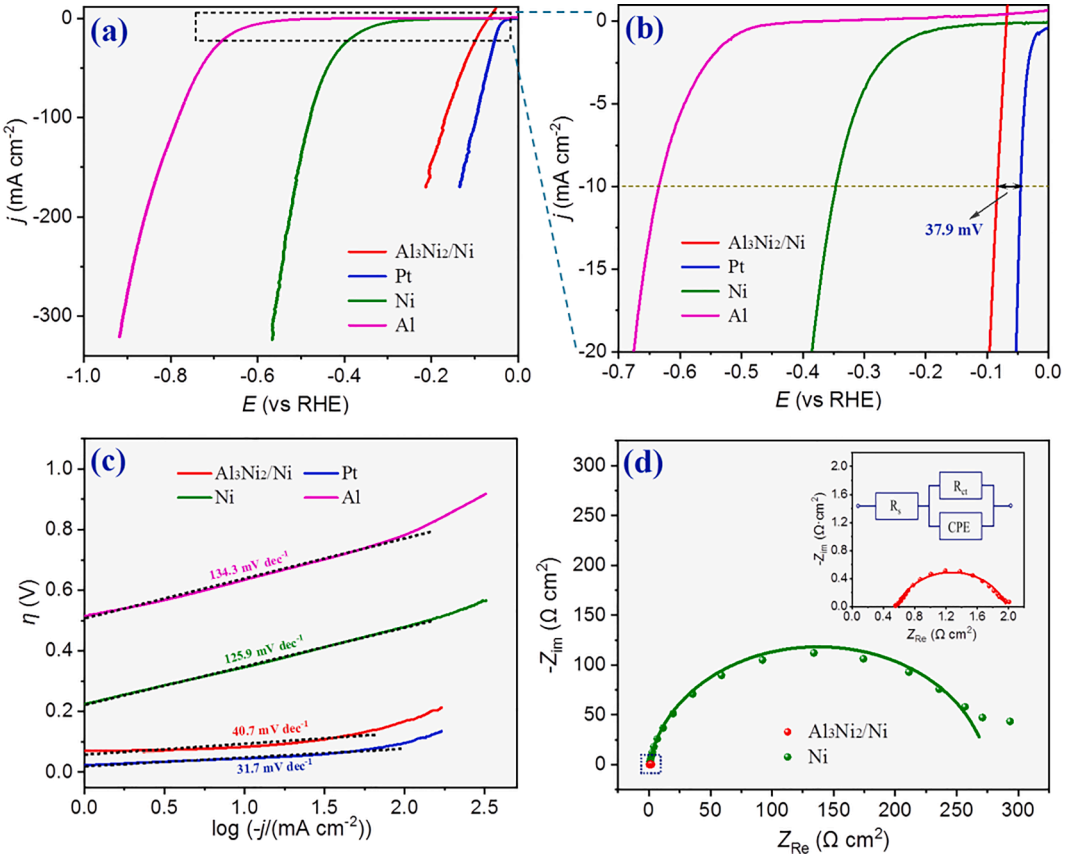

Fig. 5. Electrocatalytic performance of prepared electrodes in 0.5 M H_2SO_4: (a) IR-corrected polarization curves of Al_3Ni_2/Ni, commercial Pt, Ni and Al; (b) zoom-in image of (a) showing overpotentials at current densities of 10 mA cm^{-2} and 20 mA cm^{-2}; (c) Tafel plots derived from the polarization curves in (a); (d) Nyquist plots of Al_3Ni_2/Ni and Ni electrodes measured under overpotential of −75 mV, with inset showing the zoom-in image at high frequency and equivalent circuit used.

through the Tafel equation

$$\eta = a + b\log|j| \quad (11)$$

where a, b and j denotes the intercept, Tafel slope and current density, respectively. Normally, a smaller Tafel slope implies a more efficient kinetics of hydrogen evolution at a constant increase of overpotential [68]. As shown in Fig. 5c and Table S4, the fitted Tafel slope of the as-fabricated electrode is only 40.7 mV dec^{-1}, which is much lower than those of nickel (125.9 mV dec^{-1}) and aluminum (134.3 mV dec^{-1}), and is very close to that of Pt (31.7 mV dec^{-1}).

In principle, the HER occurring on the surface of electrode is considered as a combination of two successive steps in acidic solutions: a step of electrochemical adsorption of hydrogen (Volmer reaction) followed by an electrochemical desorption step (Heyrovsky reaction) or a chemical desorption step (Tafel reaction). The accepted reaction mechanisms can be described as follows:

(1) Volmer reaction (electrochemical adsorption of hydrogen)

$$H^+ + M^* + e^- \rightarrow M\text{-}H_{ads} \quad (12)$$

(2) Heyrovsky reaction (electrochemical desorption of hydrogen)

$$M\text{-}H_{ads} + H^+ + e^- \rightarrow M^* + H_2 \quad (13)$$

Or Tafel reaction (chemical desorption of hydrogen)

$$M\text{-}H_{ads} + M\text{-}H_{ads} \rightarrow 2M^* + H_2 \quad (14)$$

where M stands for the catalyst material, * denotes the active site for HER, and H_{ads} represents the hydrogen atom adsorbed on the catalyst. The Tafel slope, an intrinsic characteristic of the electrocatalyst, depends on the rate-determining step during HER process. Normally, a Tafel slope of ~ 120 mV dec^{-1} suggests that the rate-determining step is Volmer reaction, whereas Tafel slopes of 40 and 30 mV dec^{-1} implies Heyrovsky and Tafel reactions, respectively [69,70]. Such a small Tafel slope reveals that a high current density can be delivered at a low overpotential, leading to the favorable electrocatalytic kinetics on the as-fabricated electrode for HER. The value of Tafel slope for the as-fabricated electrode also reveals that the Heyrovsky reaction acts as the rate-determining step during the HER process and the HER process undergoes the Volmer-Heyrovsky pathway. Meanwhile, it should be noted that the as-fabricated electrode surprisingly exhibits an extremely low Tafel slope comparable to commercial Pt (a reasonably low value of 31.7 mV dec^{-1}). This is presumably correlated with the adsorbability of the generated hydrogen bubbles on the electrodes. As can be seen from Fig. S6, at a current density of 100 mA cm^{-2}, the generated hydrogen bubbles are staying on the surface of the Pt electrode until they grows to a critical size, while numerous tiny hydrogen bubbles fly off the as-fabricated electrode immediately after their formation. Owing to less resistance from hydrogen bubbles, the migration of H^+ speeds up and more absorbed hydrogen atoms will then be formed on the catalyst, consequently accelerating the Heyrovsky reaction in the HER processes, as illustrated by the Eq. (14). Besides, the exchange current densities (j_0), an evaluation index reflecting the surface reaction activation energy of the catalyst, were also further measured by extrapolating the Tafel plots, as shown in Fig. S7. The Al_3Ni_2/Ni electrode exhibits a higher j_0 value (0.062 mA cm^{-2}) than those of nickel (0.017 mA cm^{-2}), and aluminum (1.8×10^{-4} mA cm^{-2}), further confirming an outstanding inherent HER reaction kinetics.

Another crucial factor affecting the HER kinetics for a catalyst is the charge transfer resistance (R_{ct}) at the electrode/electrolyte interface, which can be quantitatively determined by fitting the Nyquist plots based on EIS. Fig. 5d shows the Nyquist plots of nickel and the as-fabricated Al_3Ni_2/Ni electrode fitted with an equivalent circuit (inset of Fig. 5d) incorporating a resistor (R_s) in series with a parallel combination of R_{ct} and a constant phase element (CPE). R_s is the ohmic resistance mainly originating from electrolyte and all contact resistances, and can be read out from the intersection of the Nyquist plot high-frequency with x-axis [71]. R_{ct} can be calculated from the semicircle diameter of Nyquist plot [71]. The quantitative values acquired from the fitted curves are summarized in Table S4. At the overpotential of 75 mV, although having the roughly equivalent values of R_s, the calculated R_{ct} for the as-fabricated electrode is merely 1.411 Ω cm^2, which is much lower than that of pure nickel (274.1 Ω cm^2), implying an extremely low resistance for electron transport across the as-fabricated electrode/electrolyte interface. The atom and electron rearrangement created by doping Al into Ni expedites the charge transfer across the electrode/electrolyte interface [72] because Ni can get additional electrons from adjacent Al atoms [56], and thus definitely leads to a rapid Faradaic process and thus superior HER kinetics on the as-fabricated electrode.

As an excellent catalytic electrode used for practical application, it must maintain long-term stability of operation without obvious degradation and frequent replacement. Thus, the stability and durability of the as-fabricated electrode were further examined through continuous galvanostatic electrolysis in 0.5 M H_2SO_4 solution under the current density of 10 mA cm^{-2} for a period of 36 h, as shown in Fig. 6a. The HER overpotential is slowly increasing from approximately −80 mV to −120 mV within the initial 6 h, which possibly results from the gradually decreased concentration of H^+ around the electrode due to the continuous depletion and the restricted diffusion of H^+ ions during electrolysis, without the stirring or refreshing the electrolyte. Afterwards, it appears to level off at around −140 mV to drive a fixed cathodic current of 10 mA cm^{-2} in the subsequent 30 h, displaying the praiseworthy stability and durability, which could be ascribed to the formation of passive oxide film on the Al_3Ni_2/Ni electrode to inhibit the further dissolution of the alloy in H_2SO_4 solution. Subsequently, the catalytic activity of the as-fabricated electrode after durability test was reassessed in the refreshed electrolyte. As anticipated, the catalytic activity of the electrode shows no degradation after a long-time electrolysis, but indicates even a slight improvement (Fig. 6b), with an HER overpotential decrease of 11.4 mV and 14.1 mV to gain a current density of 10 and 100 mA cm^{-2}, respectively. Fig. 6c depicts that the Tafel slope maintains a low value (39.5 mV dec^{-1}), corresponding to the favorable kinetics of as-fabricated electrode during HER. Consistent with the polarization curve in Fig. 6b and the Tafel plot in Fig. 6c, the small R_{ct} exhibits the impressively fast charge transfer of the electrode for HER even after a period of 36 h electrolysis, as exhibited in Fig. 6d and Table S4.

To examine the physicochemical structures of Al_3Ni_2/Ni electrode after a long-term HER test, the chemical structure and surface morphology of Al_3Ni_2/Ni were probed with XRD, SEM-EDS and XPS. Owing to the dissolution of Al (Fig. S6), the Ni-richer phase of AlNi has become one of the main phases in the alloy deposit after 36 h durability test, as shown in Fig. 7a. It is clear that the surface of the electrode becomes relatively loose (Fig. 7b), resulting from the slow dissolution of Al as well as the long-time impact of the rapid generation of hydrogen bubbles. In accordance, the proportion of Al in the alloy deposit also decreases somewhat (Fig. 7c). However, the intermetallic Al_3Ni_2 still exists as one of the main phases in the deposit and the electrode is still closely covered by numerous micro-sized particles and retains the original 3D cauliflower-like morphology very well. The rough surface accompanied with the newly formed channels is likely supportive to the favorable catalytic performance for the as-fabricated electrode during long-term HER process. In this regard, the slight dissolution of Al during the HER process will not cause severe adverse impacts, but can be beneficial to enhance the catalytic performance of the electrode. The XPS spectrum (Fig. 7d) indicates that the surface of the electrode after 36 h continuous electrolysis still comprises Al, Ni, O and C elements. Noticeably, the XPS signal of C 1 s becomes much remarkable. It can be attributed to the carbon contamination from the graphite counter electrode during the long-term electrolysis. The peaks of Ni 2p and Ni 3p show negligible shifts (Fig. 7e). The Al 2p spectrum (Fig. 7f) reveals two binding energy peaks at 72.2 and 74.8 eV, which are still the characteristics of Al element associated with metallic Al and Al_2O_3,

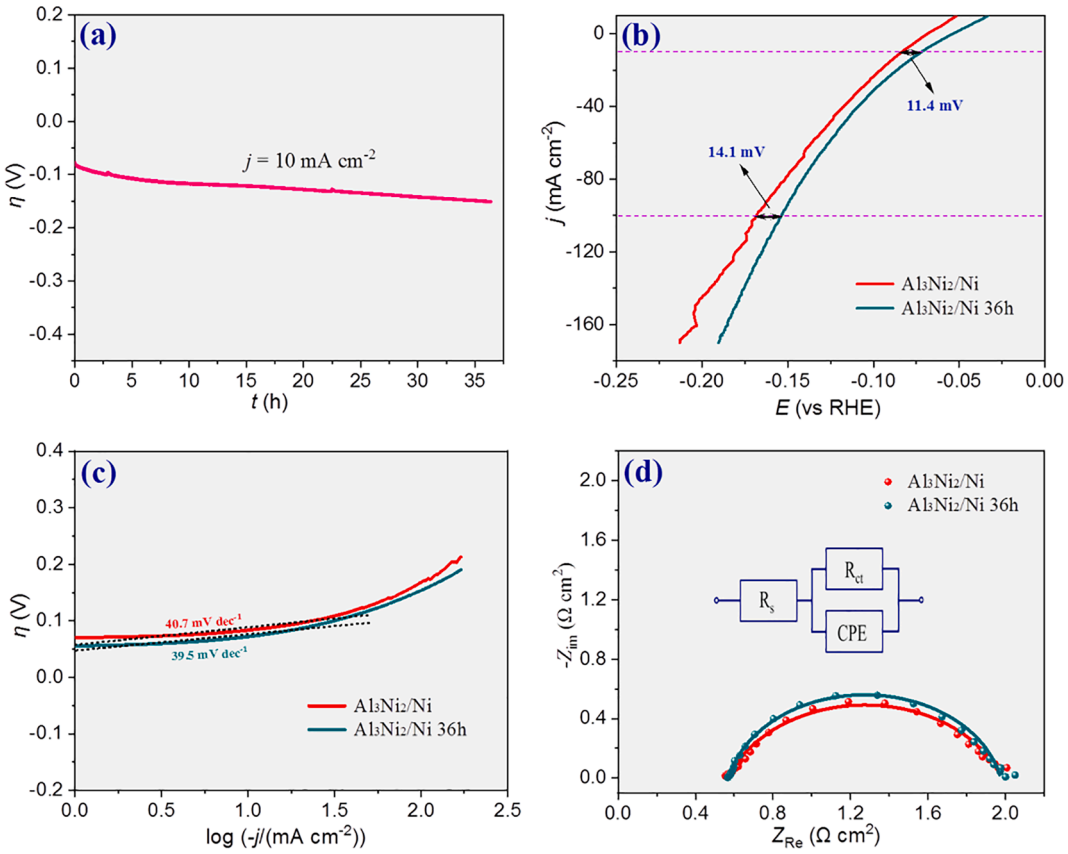

Fig. 6. (a) Chronopotentiometric (η-t) curve of the Al_3Ni_2/Ni electrode recorded at 10 mA cm^{-2}, with the inset of the surface morphology of the electrode after a continuous galvanostatic electrolysis for 36 h; (b) The polarization curves, (c) the corresponding Tafel plots and (d) Nyquist plots of the Al_3Ni_2/Ni electrode measured under overpotential of −75 mV before and after continuous galvanostatic electrolysis in 0.5 M H_2SO_4 for 36 h.

respectively [73,74]. The unchanged chemical states of Ni and Al on the electrode surface further confirm that the fabricated Al_3Ni_2/Ni electrode is fairly stable during the HER process.

3.6. Catalysis mechanism of the Al_3Ni_2/Ni electrode for HER

The Al_3Ni_2/Ni electrode fabricated directly by molten salt electrolysis exhibits excellent catalytic performance for HER and is superior to the most typical Ni-based catalytic electrodes (Table S5 and Fig. S8). Generally, the catalytic performance of an electrode for water splitting is associated with many factors, including the chemical nature of the catalyst, the surface micromorphology, the charge transfer resistance and the adsorbability of the generated bubbles on the electrode, etc. Based on the above investigations, the outstanding HER efficiency of the as-fabricated Al_3Ni_2/Ni electrode is likely derived from the synergetic effects of these four factors. Firstly, the high intrinsic catalytic activity and the favorable (100) atomic plane of the synthesized Al_3Ni_2 intermetallic provide massive active sites, facilitating the HER process [75]. Secondly, the 3D cauliflower-like surface morphology comprising of numerous nano- and microsized Al_3Ni_2 particles produced by molten salt electrodeposition, enlarges the interfacial contact of the catalyst with electrolyte, which not only efficiently stimulates the charge transfer, but also favors the mass transfer. Thirdly, the electrical resistance of the self-standing Al_3Ni_2/Ni electrode can be minimized due to nonuse of any insulating polymer binders. More importantly, the electronic structure of Al_3Ni_2 can be refined by Al doping [29] because of electron transfer from Al atoms to Ni atoms and the consequent redistribution of the local electrons on Ni active sites. Besides, Al doping will also influence the surface adsorption energy of reactants and the Al_3Ni_2/Ni electrode and then facilitate the interaction between the reactant molecules and Ni active sites during the HER process [31]. As a result, the Al doping enhances the charge transfer across the electrode/electrolyte interface, resulting in the super HER kinetics comparable to Pt. Lastly, the Al_3Ni_2/Ni electrode fabricated via electrodeposition in molten salts appears to be repulsive to the generated hydrogen bubbles, making it more beneficial for H^+ access and penetration. Moreover, the favorable adhesion of solid Al_3Ni_2 grown directly on Ni substrate also benefits the mechanical properties and catalytic stability. The possible mechanism of electrocatalytic hydrogen splitting on Al_3Ni_2/Ni electrode is proposed in Fig. 8. All of the above aspects are synergistically responsible for the fast electron and mass transfer, leading to the high efficiency and durability for HER.

4. Conclusions

In summary, a facile one-step approach to directly fabricating self-standing Al_3Ni_2/Ni catalytic electrode for more efficient water splitting was developed via molten salt electrodeposition. The underpotential deposition of aluminum on Ni-substrate at a temperature of 700 ℃ results in the formation of various Al-Ni intermetallic compounds. By controlling the applied potential at −1.20 V (vs Ag/AgCl) and electrodeposition time of 5 h, a uniform layer of Al_3Ni_2 with thickness up to 100 μm was deposited tightly onto the nickel substrate. Due to the rapid nucleation rate during molten salt electrodeposition, nano and microsized Al_3Ni_2 grains generate onto the electrode substrate and grow into 3D cauliflower-like particles, exposing massive HER active sites. The as-fabricated Al_3Ni_2/Ni electrode can be directly used as the cathode for water splitting. Experiments of water electrolysis with the fabricated Al_3Ni_2/Ni as cathode in 0.5 M H_2SO_4 solution exhibit a low overpotential of 83.4 mV at a current density of 10 mA cm^{-2}, a small

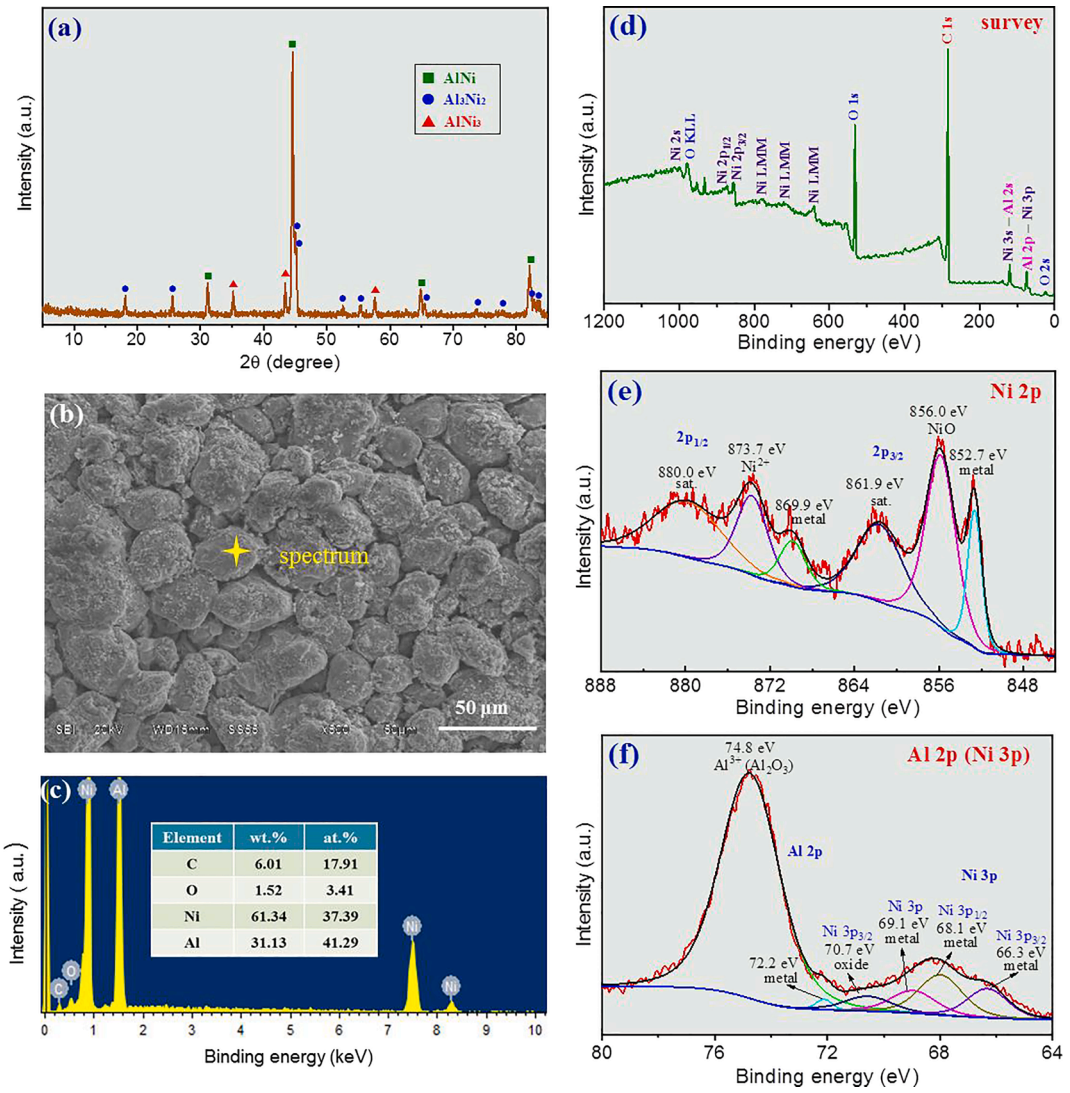

Fig. 7. (a) XRD pattern, (b) SEM image, (c) EDS analysis and (d-f) XPS spectra of the Al_3Ni_2/Ni electrode after continuous galvanostatic electrolysis at 10 mA cm^{-2} in 0.5 M H_2SO_4 solution for 36 h.

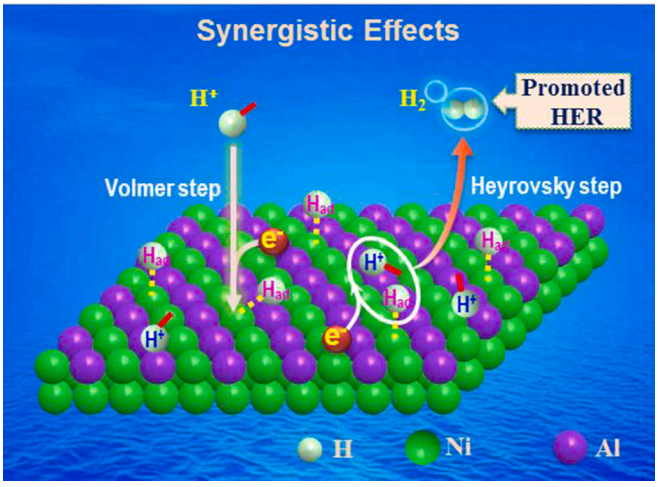

Fig. 8. Schematic illustration of the electrocatalytic mechanism toward HER for Al_3Ni_2/Ni cathode in acid media.

Tafel slope of 40.7 mV dec^{-1}, and commendable long-term durability. The prominent catalytic performance of the Al_3Ni_2/Ni electrode can be ascribed to the abundant active sites of the Al_3Ni_2 phase, the high specific surface area of nano- and microsized Al_3Ni_2 grains, the low resistance resulting from the Al doping and nonuse of insulating binders, and the effortless hydrogen bubble escape due to the feeble adsorbability to the electrode surface. Overall, this work provides a new approach to the direct fabrication of self-standing Al-Ni catalytic electrode, with controlled phase composition and nano/microstructure morphology, to achieve highly efficient water splitting. The findings will provide further insights for understanding the HER mechanism in acid electrolyte.

Declaration of Competing Interest

The authors declare that they have no known competing financial interests or personal relationships that could have appeared to influence the work reported in this paper.

Acknowledgements

This work was financially supported by the National Natural Science Foundation of China (51204002 and 51904003), Anhui Provincial Natural Science Foundation (2008085ME170), Developing Program

Foundation for the Excellent Youth Talents of Higher Education of Anhui Province (gxyq2018012), and Foundation of Anhui Province Key Laboratory of Metallurgical Engineering & Resources Recycling (SKF19-05).

Appendix A. Supplementary data

Supplementary data to this article can be found online at https://doi.org/10.1016/j.cej.2021.131743.

References

[1] Z. Pan, Q. Ding, L. Yao, S. Huang, S. Xing, J. Liu, J. Chen, J. Zhai, Simultaneously enhanced discharge energy density and efficiency in nanocomposite film capacitors utilizing two-dimensional $NaNbO_3$@Al_2O_3 platelets, Nanoscale 11 (2019) 10546–10554.

[2] W. Weng, B. Jiang, Z. Wang, W. Xiao, In situ electrochemical conversion of CO_2 in molten salts to advanced energy materials with reduced carbon emissions, Sci. Adv. 6 (2020) eaay9278.

[3] C. Wei, Y. Sun, G.G. Scherer, A.C. Fisher, M. Sherburne, J.W. Ager, Z.J. Xu, Surface composition dependent ligand effect in tuning the activity of nickel–copper bimetallic electrocatalysts toward hydrogen evolution in alkaline, J. Am. Chem. Soc. 142 (2020) 7765–7775.

[4] W. Yang, S. Chen, Recent progress in electrode fabrication for electrocatalytic hydrogen evolution reaction: A mini review, Chem. Eng. J. 393 (2020), 124726.

[5] N. Armaroli, V. Balzani, The future of energy supply: challenges and opportunities, Angew. Chem. Int. Ed. 46 (1-2) (2007) 52–66.

[6] J.D. Holladay, J. Hu, D.L. King, Y. Wang, An overview of hydrogen production technologies, Catal. Today 139 (4) (2009) 244–260.

[7] Zeyu Fan, Wei Xiao, electrochemical splitting of methane in molten salts to produce hydrogen, Angew. Chem. Int. Ed. 60 (14) (2021) 7664–7668.

[8] J. Zhang, Z. Zhang, Y. Yao, Y. Ma, Y. Yang, Y. Chen, Z. Cheng, In situ construction of Ni enriched porous NiAl as long-lived electrode for hydrogen evolution at high current densities, Appl. Surf. Sci. 489 (2019) 435–445.

[9] M. Carmo, D.L. Fritz, J. Mergel, D. Stolten, A comprehensive review on PEM water electrolysis, Int. J. Hydrogen Energ. 38 (12) (2013) 4901–4934.

[10] X. Liang, J. Xiao, W. Weng, W. Xiao, Electrochemical reduction of carbon dioxide and iron oxide in molten salts to Fe/Fe_3C modified carbon for electrocatalytic oxygen evolution, Angew. Chem. Int. Ed. 60 (4) (2021) 2120–2124.

[11] P.V. Cherepanov, M. Ashokkumar, D.V. Andreeva, Ultrasound assisted formation of Al–Ni electrocatalyst for hydrogen evolution, Ultrason. Sonochem. 23 (2015) 142–147.

[12] F. Rosalbino, D. Macciò, A. Saccone, E. Angelini, S. Delfino, Fe-Mo-R (R = rare earth metal) crystalline alloys as a cathode material for hydrogen evolution reaction in alkaline solution, Int. J. Hydrogen Energ. 36 (2011) 1965–1973.

[13] G. Cao, N. Xu, Z. Chen, Q. Kang, H. Dai, P. Wang, Cobalt-tungsten-boron as an active electrocatalyst for water electrolysis, ChemistrySelect 2 (21) (2017) 6187–6193.

[14] I. Ledezma-Yanez, W.D.Z. Wallace, P. Sebastián-Pascual, V. Climent, J.M. Feliu, M. T.M. Koper, Interfacial water reorganization as a pH-dependent descriptor of the hydrogen evolution rate on platinum electrodes, Nat. Energy 2 (2017) 17031–17037.

[15] H. Ashassi-Sorkhabi, B. Rezaei-Moghadam, E. Asghari, R. Bagheri, Z. Hosseinpour, Fabrication of bridge like Pt@MWCNTs/CoS_2 electrocatalyst on conductive polymer matrix for electrochemical hydrogen evolution, Chem. Eng. J. 308 (2017) 275–288.

[16] Q. Sun, Y. Dong, Z. Wang, S. Yin, C. Zhao, Synergistic nanotubular copper-doped nickel catalysts for hydrogen evolution reactions, Small 14 (2018) 1704137.

[17] B. Hinnemann, P.G. Moses, J. Bonde, K.P. Jorgensen, J.H. Nielsen, S. Horch, I. Chorkendorff, J.K. Norskov, Biomimetic hydrogen evolution: MoS_2 nanoparticles as catalyst for hydrogen evolution, J. Am. Chem. Soc. 127 (2005) 5308–5309.

[18] Y. Li, Z. Dong, L. Jiao, Multifunctional transition metal-based phosphides in energy related electrocatalysis, Adv. Energy Mater. 10 (2020) 1902104.

[19] J. Greeley, T.F. Jaramillo, J. Bonde, I. Chorkendorff, J.K. Nørskov, Computational high-throughput screening of electrocatalytic materials for hydrogen evolution, Nat. Mater. 5 (11) (2006) 909–913.

[20] X. Zou, Y. Zhang, Noble metal-free hydrogen evolution catalysts for water splitting, Chem. Soc. Rev. 44 (15) (2015) 5148–5180.

[21] M.S. Faber, S. Jin, Earth-abundant inorganic electrocatalysts and their nanostructures for energy conversion applications, Energ. Environ. Sci. 7 (11) (2014) 3519–3542.

[22] Y. Shi, B. Zhang, Recent advances in transition metal phosphide nanomaterials: synthesis and applications in hydrogen evolution reaction, Chem. Soc. Rev. 45 (2016) 1529–1541.

[23] R. Shen, J. Xie, Q. Xiang, X. Chen, J. Jiang, X. Li, Ni-based photocatalytic H_2-production cocatalysts, Chinese J. Catal. 40 (2019) 240–288.

[24] H. Zhou, Y. Wang, R. He, F. Yu, J. Sun, F. Wang, Y. Lan, Z. Ren, S. Chen, One-step synthesis of self-supported porous $NiSe_2$/Ni hybrid foam: an efficient 3D electrode for hydrogen evolution reaction, Nano Energy 20 (2016) 29–36.

[25] P. Kuang, M. He, H. Zou, J. Yu, K. Fan, 0D/3D MoS_2-NiS_2/N-doped graphene foam composite for efficient overall water splitting, Appl. Catal. B-Environ. 254 (2019) 15–25.

[26] H. Dong, T. Lei, Y. He, N. Xu, B. Huang, C.T. Liu, Electrochemical performance of porous Ni_3Al electrodes for hydrogen evolution reaction, Int. J. Hydrogen Energ. 36 (19) (2011) 12112–12120.

[27] P. Kuang, T. Tong, K. Fan, J. Yu, In situ fabrication of Ni-Mo bimetal sulfide hybrid as an efficient electrocatalyst for hydrogen evolution over a wide pH range, ACS Catal. 7 (9) (2017) 6179–6187.

[28] P. Los, A. Rami, A. Lasia, Hydrogen evolution reaction on Ni–Al electrodes, J. Appl. Electrochem. 23 (1993) 135–140.

[29] J.L. Lado, X. Wang, E. Paz, E. Carbó-Argibay, N. Guldris, C. Rodríguez-Abreu, L. Liu, K. Kovnir, Y.V. Kolen'ko, Design and synthesis of highly active Al-Ni-P foam electrode for hydrogen evolution reaction, ACS Catal. 5 (2015) 6503–6508.

[30] J.S. Sun, Z. Wen, L.P. Han, Z.W. Chen, X.Y. Lang, Q. Jiang, Nonprecious intermetallic Al_7Cu_4Ni nanocrystals seamlessly integrated in freestanding bimodal nanoporous copper for efficient hydrogen evolution catalysis, Adv. Funct. Mater. 28 (2018) 1706127.

[31] Y. Zhou, H. Liu, S. Zhu, Y. Liang, S. Wu, Z. Li, Z. Cui, C. Chang, X. Yang, A. Inoue, Highly efficient and self-standing nanoporous NiO/Al_3Ni_2 electrocatalyst for hydrogen evolution reaction, ACS Appl. Energ. Mater. 2 (2019) 7913–7922.

[32] T. Czeppe, S. Wierzbinski, Structure and mechanical properties of NiAl and Ni_3Al-based alloys, Int. J. Mech. Sci. 42 (8) (2000) 1499–1518.

[33] H.J Grabke, Oxidation of NiAl and FeAl, Intermetallics 7 (10) (1999) 1153–1158.

[34] H.X. Dong, Y.H. He, Y. Jiang, L. Wu, J. Zou, N.P. Xu, B.Y. Huang, C.T. Liu, Effect of Al content on porous Ni_3Al alloys, Mat. Sci. Eng. A 528 (2011) 4849–4855.

[35] L. Wu, H.X. Dong, Y.H. He, Preparation and corrosion resistance in KOH solution of porous Ni_3Al, Chinese J. Mat. Res. 25 (2011) 118–123 (in Chinese).

[36] H. Sun, Z. Yan, F. Liu, W. Xu, F. Cheng, J. Chen, Self-supported transition-metal based electrocatalysts for hydrogen and oxygen evolution, Adv. Mater. 32 (2020) 1806326.

[37] J. Liu, D. Zhu, Y. Zheng, A. Vasileff, S. Qiao, Self-supported earth-abundant nanoarrays as efficient and robust electrocatalysts for energy-related reactions, ACS Catal. 8 (7) (2018) 6707–6732.

[38] X. Shang, X. Zhang, J. Xie, B. Dong, J. Chi, B. Guo, M. Yang, Y. Chai, C. Liu, Double catalytic-site engineering of nickel-based electrocatalysts by group VB metals doping coupling with in-situ cathodic activation for hydrogen evolution, Appl. Catal. B-Environ. 258 (2019), 117984.

[39] S. Anantharaj, S.R. Ede, K. Sakthikumar, K. Karthick, S. Mishra, S. Kundu, Recent trends and perspectives in electrochemical water splitting with an emphasis on sulfide, selenide, and phosphide catalysts of Fe Co, and Ni: a review, ACS Catal. 6 (12) (2016) 8069–8097.

[40] W. Xu, S. Zhu, Y. Liang, Z. Cui, X. Yang, A. Inoue, A nanoporous metal phosphide catalyst for bifunctional water splitting, J. Mater. Chem. A 6 (2018) 5574–5579.

[41] W. Weng, J. Yang, J. Zhou, D. Gu, W. Xiao, Template-free electrochemical formation of silicon nanotubes from silica, Adv. Sci. 7 (2020) 2001492.

[42] T. Lv, J. Xiao, W. Weng, W. Xiao, Electrochemical fixation of carbon dioxide in molten salts on liquid zinc cathode to zinc@graphitic carbon spheres for enhanced energy storage, Adv. Energy Mater. 10 (2020) 2002241.

[43] J. He, Z. Hua, H. Liu, L. Xu, S. He, Y. Yang, Z. Zhao, Redox behavior of yttrium and electrochemical formation of Y−Al alloys in molten chlorides, J. Electrochem. Soc. 165 (2018) E598–E603.

[44] W. Weng, J. Zhou, D. Gu, W. Xiao, Thermoelectrochemical formation of Fe/Fe_3C@hollow N-doped carbon in molten salts for enhanced catalysis, J. Mater. Chem. A 8 (2020) 4800–4806.

[45] W. Weng, S. Wang, W. Xiao, X.W. Lou, Direct conversion of rice husks to nanostructured SiC/C for CO_2 photoreduction, Adv. Mater. 32 (2020) 2001560.

[46] Z. Hua, H. Liu, J. Wang, J. He, S. Xiao, Y. Xiao, Y. Yang, Electrochemical behavior of neodymium and formation of Mg–Nd alloys in molten chlorides, ACS Sustain. Chem. Eng. 5 (2017) 8089–8096.

[47] Y. Wang, R. Lin, G. Ye, H. He, H. Tang, Y. Jia, Progress of Ag /AgCl reference electrode in high-temperature chloride molten salt, Mod. Chem. Ind. 35 (2015) 21–25 (in Chinese).

[48] H. Tang, Y.D. Yan, M.L. Zhang, X. Li, Y. Huang, Y.L. Xu, Y. Xue, W. Han, Z. J. Zhang, $AlCl_3$-aided extraction of praseodymium from Pr_6O_{11} in LiCl–KCl eutectic melts, Electrochim. Acta 88 (2013) 457–462.

[49] Y. Peng, Z. Chen, Y. Bai, Q. Pei, W. Li, C. Diao, X. Li, S. Li, S. Dong, Electrochemical behavior of Al(III) and formation of different phases Al-Ni alloys deposits from LiCl-KCl-$AlCl_3$ molten salt, Materials 11 (2018) 2113.

[50] X. Li, Y.D. Yan, M.L. Zhang, H. Tang, D.B. Ji, W. Han, Y. Xue, Z.J. Zhang, Electrochemical reduction of Tm on Mg electrodes and co-reduction of Mg, Li and Tm on W electrodes, Electrochim. Acta 135 (2014) 327–335.

[51] A.J. Bard, L.R. Faulkner, Electrochemical methods: fundamentals and applications, John Wiley & Sons, New York, 2001.

[52] S. Wang, W. Han, M. Zhang, M. Li, X. Yang, Y. Sun, Electrochemical behaviour of magnesium(II) on Ni electrode in LiCl-KCl eutectic, Chem. Res. Chinese U. 34 (2018) 107–112.

[53] Y. Castrillejo, P. Fernández, J. Medina, M. Vega, E. Barrado, Chemical and electrochemical extraction of ytterbium from molten chlorides in pyrochemical processes, Electroanal. 23 (2011) 222–236.

[54] S. Wang, B. Wei, M. Li, W. Han, M. Zhang, X. Yang, Y. Sun, Electrochemical behavior of Dy(III) on bismuth film electrode in eutectic LiCl-KCl melts, J. Rare Earth. 36 (2018) 1007–1014.

[55] Z. Zhu, X. Wu, Z. Hua, L. Xu, S. He, A. Geng, Y. Yang, Z. Zhao, Electrochemical behavior of Dy(III) and formation of Dy-Zn alloy by co-reduction with Zn(II) in eutectic NaCl-KCl melts, J. Electrochem. Soc. 167 (2020), 122509.

[56] Z. Li, W. Niu, L. Zhou, Y. Yang, Phosphorus and aluminum codoped porous NiO nanosheets as highly efficient electrocatalysts for overall water splitting, ACS Energy Lett. 3 (2018) 892–898.

[57] Y. Castrillejo, A. Vega, M. Vega, P. Hernández, J.A. Rodriguez, E. Barrado, Electrochemical formation of Sc-Al intermetallic compounds in the eutectic LiCl-KCl. Determination of thermodynamic properties, Electrochim. Acta 118 (2014) 58–66.
[58] L.X. Luo, Y.L. Liu, N. Liu, L. Wang, L.Y. Yuan, Z.F. Chai, W.Q. Shi, Electrochemical and thermodynamic properties of Nd(III)/Nd(0) couple at liquid Zn electrode in LiCl-KCl melt, Electrochim. Acta 191 (2016) 1026–1036.
[59] Y. Zeng, Y. Meng, Z. Lai, X. Zhang, M. Yu, P. Fang, M. Wu, Y. Tong, X. Lu, An ultrastable and high-performance flexible fiber-shaped Ni–Zn battery based on a Ni–NiO heterostructured nanosheet cathode, Adv. Mater. 29 (2017) 1702698.
[60] R. Kumar, T. Bhuvana, P. Rai, A. Sharma, Highly sensitive non-enzymatic glucose detection using 3-D $Ni_3(VO_4)_2$ nanosheet arrays directly grown on Ni foam, J. Electrochem. Soc. 165 (2018) B1–B8.
[61] T. Wei, F. Yan, J. Tian, Characterization and wear-and corrosion-resistance of microarc oxidation ceramic coatings on aluminum alloy, J. Alloy. Compd. 389 (2005) 169–176.
[62] M.S. Selim, P.J. Mo, Y.P. Zhang, Z. Hao, H. Wen, Controlled-surfactant-directed solvothermal synthesis of γ-Al_2O_3 nanorods through a boehmite precursor route, Ceram. Int. 46 (7) (2020) 9289–9296.
[63] K. Yasuda, S. Kobayashi, T. Nohira, R. Hagiwara, Electrochemical formation of Dy–Ni alloys in molten NaCl–KCl–$DyCl_3$, Electrochim. Acta 106 (2013) 293–300.
[64] G. Lu, G. Zangari, Corrosion resistance of ternary Ni-P based alloys in sulfuric acid solutions, Electrochim. Acta 47 (18) (2002) 2969–2979.
[65] J. Tang, Y. Wang, Q. Zhu, M. Chamas, H. Wang, J. Qiao, Y. Zhu, B. Normand, Passivation behavior of a Zr60Cu20Ni8Al7Hf3Ti2 bulk metallic glass in sulfuric acid solutions, Int. J. Electrochem. Sci. 13 (2018) 6913–6929.
[66] W.R. Osório, J.E. Spinelli, C.R.M. Afonso, L.C. Peixoto, A. Garcia, Electrochemical corrosion behaviour of gas atomized Al–Ni alloy powders, Electrochim. Acta 69 (2012) 371–378.
[67] G.H. Han, H. Kim, J. Kim, J. Kim, S.Y. Kim, S.H. Ahn, Micro-nanoporous MoO_2@CoMo heterostructure catalyst for hydrogen evolution reaction, Appl. Catal. B-Environ. 270 (2020), 118895.
[68] D. Wang, X. Zhang, S. Bao, Z. Zhang, H. Fei, Z. Wu, Phase engineering of a multiphasic 1T/2H MoS_2 catalyst for highly efficient hydrogen evolution, J. Mater. Chem. A 5 (2017) 2681–2688.
[69] J. Xie, H. Zhang, S. Li, R. Wang, X. Sun, M. Zhou, J. Zhou, X.W. Lou, Y. Xie, Defect-rich MoS_2 ultrathin nanosheets with additional active edge sites for enhanced electrocatalytic hydrogen evolution, Adv. Mater. 25 (2013) 5807–5813.
[70] Y. Li, H. Wang, L. Xie, Y. Liang, G. Hong, H. Dai, MoS_2 nanoparticles grown on graphene: an advanced catalyst for the hydrogen evolution reaction, J. Am. Chem. Soc. 133 (2011) 7296–7299.
[71] J. Zhang, Z. Zhang, Y. Ji, J. Yang, K. Fan, X. Ma, C. Wang, R. Shu, Y. Chen, Surface engineering induced hierarchical porous $Ni_{12}P_5$-Ni_2P polymorphs catalyst for efficient wide pH hydrogen production, Appl. Catal. B-Environ. 282 (2021), 119609.
[72] A. Chunduri, S. Gupta, O. Bapat, A. Bhide, R. Fernandes, M.K. Patel, V. Bambole, A. Miotello, N. Patel, A unique amorphous cobalt-phosphide-boride bifunctional electrocatalyst for enhanced alkaline water-splitting, Appl. Catal. B-Environ. 259 (2019), 118051.
[73] Y. Park, J. Lee, S.K. Lee, Photoelectron spectroscopy study of the electronic structures of Al/MgF_2/tris-(8-hydroxyquinoline) aluminum interfaces, Appl. Phys. Lett. 79 (2001) 105–107.
[74] H. Liu, Q. Mei, S. Li, Y. Yang, Y. Wang, H. Liu, L. Zheng, P. An, J. Zhang, B. Han, Selective hydrogenation of unsaturated aldehydes over Pt nanoparticles promoted by the cooperation of steric and electronic effects, Chem. Commun. 54 (2018) 908–911.
[75] P.V. Cherepanov, I. Melnyk, E.V. Skorb, P. Fratzl, E. Zolotoyabko, N. Dubrovinskaia, L. Dubrovinsky, Y.S. Avadhut, J. Senker, L. Leppert, S. Kümmelg, D.V. Andreeva, The use of ultrasonic cavitation for near-surface structuring of robust and low-cost AlNi catalysts for hydrogen production, Green Chem. 17 (2015) 2745–2749.